

# 1-D CNN deep learning of impedance signals for damage monitoring in concrete anchorage

Quoc-Bao Ta<sup>1a</sup>, Quang-Quang Pham<sup>1,2b</sup>, Ngoc-Lan Pham<sup>1c</sup> and Jeong-Tae Kim<sup>\*1</sup>

<sup>1</sup>Department of Ocean Engineering, Pukyong National University, Nam-gu, Busan 48513, Republic of Korea

<sup>2</sup>Bridge and Road Department, Danang Architecture University, Da Nang 550000, Vietnam

(Received January 23, 2023, Revised March 4, 2023, Accepted March 10, 2023)

**Abstract.** Damage monitoring is a prerequisite step to ensure the safety and performance of concrete structures. Smart aggregate (SA) technique has been proven for its advantage to detect early-stage internal cracks in concrete. In this study, a 1-D CNN-based method is developed for autonomously classifying the damage feature in a concrete anchorage zone using the raw impedance signatures of the embedded SA sensor. Firstly, an overview of the developed method is presented. The fundamental theory of the SA technique is outlined. Also, a 1-D CNN classification model using the impedance signals is constructed. Secondly, the experiment on the SA-embedded concrete anchorage zone is carried out, and the impedance signals of the SA sensor are recorded under different applied force levels. Finally, the feasibility of the developed 1-D CNN model is examined to classify concrete damage features via noise-contaminated signals. The results show that the developed method can accurately classify the damaged features in the concrete anchorage zone.

**Keywords:** 1-D CNN; anchorage zone; concrete damage; convolutional neural network (CNN); damage classification; deep learning; impedance-based monitoring; smart aggregate

---

## 1. Introduction

Prestressed concrete (PSC) is widely utilized in bridge construction due to its cost-effectiveness and enhanced crack resistance compared to reinforced concrete structures. For PSC bridges, the anchorage zones play a vital role in transmitting the designed prestress force to the structures. However, over time, material deterioration, corrosion, and time-dependent prestress loss could cause a gradual decline in the structural performance of PSC members, resulting in long-term deformation. In addition, incipient concrete damage in the form of inner micro-cracks can lead to surface cracks, which typically occur in tensile regions and remain invisible at early stages. Environmental erosion can exacerbate material degradation once cracks propagate onto the surface. Severe concrete cracks in PSC bridges are a growing concern for designers, investigators, and managers (Mehrabi *et al.* 2010, Hou *et al.* 2017). Therefore, early detection of concrete cracks in PSC structures is crucial to

---

\*Corresponding author, Professor, E-mail: idis@pknu.ac.kr

<sup>a</sup>Graduate Student

<sup>b</sup>Postdoctoral Researcher

<sup>c</sup>Graduate Student

ensure structural integrity and reduce long-term maintenance costs.

Various Structural Health Monitoring (SHM) methods using vibration characteristics such as natural frequencies, mode shapes, and modal curvatures have been proposed to detect damage in PSC members (Ho *et al.* 2012, Cancelli *et al.* 2019). However, these methods utilize low modal parameters insensitive to incipient damage. On the other hand, local techniques, such as visual inspections and X-rays, have been implemented to monitor structural damage in PSC structures (Lee *et al.* 2014, Aryan *et al.* 2018). Although these methods are recognized in various applications, their sensitivity is inadequate for reliable detection of incipient damage (such as internal concrete damage) or material deterioration. Additionally, these methods can be time-consuming, costly, and even unsafe for inspectors. Strain-based methods have been used to detect structural damage by utilizing the well-established relationship between stress and strain. Among various strain sensors, fiber optic sensors are commonly used for damage monitoring due to their high durability and sensitivity (Wu *et al.* 2020). However, the fabrication of sensing-cable-embedded fiber optic sensors remains a challenge.

In demand for real-time SHM monitoring, the electromechanical impedance (EMI) technique has attracted significant attention from researchers due to its advantages, such as sensing and driving functionalities, fast response speed, stable performance, and low price (Na *et al.* 2018). The technique utilizes the coupling interaction between a PZT (lead zirconated titanate) transducer and the monitored structure to provide information about the local structural characteristics of the examined region (Liang *et al.* 1994). The technique has been extensively implemented for monitoring stress in concrete structures (Ai *et al.* 2019, Pham *et al.* 2021). Many studies propose using PZT sensors placed on the surface of concrete structures to detect changes in impedance response induced by local damage near the surface (Ai *et al.* 2019, Pham *et al.* 2021). However, those surface-mounted PZT sensors are found to be less sensitive to changes in internal concrete stress (Pham *et al.* 2021). The so-called smart aggregate (SA) sensor (Gu *et al.* 2006), which was embedded into a monitored concrete structure, has recently emerged as an alternative internal stress monitoring method. The change in internal concrete stresses and the occurrence of damage events can directly reflect on the impedance response (Pham *et al.* 2021, Wu *et al.* 2022).

In the EMI technique, the impedance features such as root-mean-square-deviation (RMSD) (Sun *et al.* 1995) and cross-correlation deviation (CCD) (Zagrai and Giurgiutiu 2002) are often used to quantify the change in impedance signal measured for stress estimation and damage detection. However, extracting meaningful impedance features from suitable frequency bands is challenging to secure damage detection's reliability. The traditional strategy requires multi-steps and is mainly based on try-and-error (Park *et al.* 2003). The prediction results depend heavily on selecting effective frequency bands and impedance features. Using hand-crafted impedance features could further cause difficulties in quantitative stress evaluation and false alarms for damage assessment (Min *et al.* 2010). In addition, the manual feature extraction may prevent the technique from a real-time operation. Therefore, there is a need to develop an alternative method for damage monitoring with automated impedance feature extraction.

In recent years, convolutional neural network (CNN)-based deep learning algorithms have emerged as efficient approaches for assessing structural conditions of civil infrastructures (Sony *et al.* 2021). While the traditional damage detection method consists of two main steps: (i) feature extraction and (2) damage identification (Yuan *et al.* 2020), a CNN-based method combines them in a single procedure (Abdeljaber *et al.* 2018). The network can directly process raw signals and autonomously learn optimal features for a damage identification task, considerably reducing the initial processing workload. Several studies explored the combination of the CNN and the

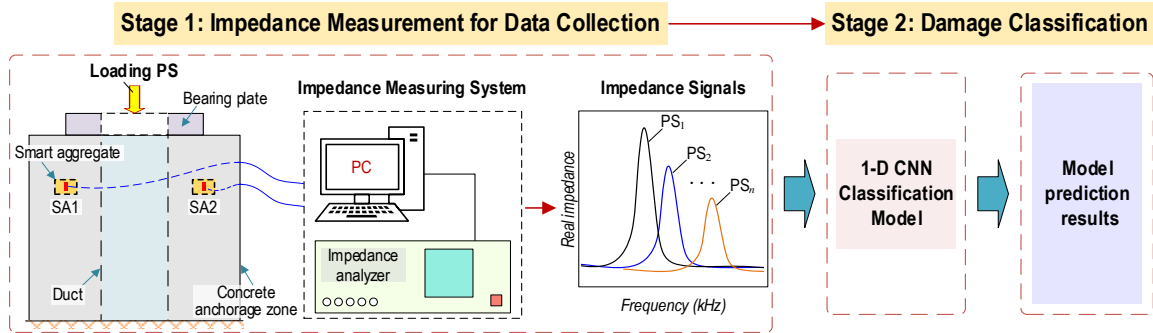


Fig. 1 Schematic of methodology

impedance-based technique for damage assessment. Nguyen *et al.* (2021) proposed a 1-D CNN model that learned impedance signatures for classifying different health conditions of a smart PZT interface. Recently, Nguyen *et al.* (2022) explored the ability of the 1-D CNN for autonomous features extraction for impedance-based prestress force prediction. Ai *et al.* (2022) proposed a 2-D CNN model to classify compressive stress and damage in concrete samples based on the admittance responses obtained from the PZT sensors surface-mounted on a concrete block. The above studies have demonstrated the applicability of CNN as an innovative algorithm for impedance-based damage detections with minimal signal preprocessing.

Despite the previous research attempts (Nguyen *et al.* 2021, Nguyen *et al.* 2022, Ai *et al.* 2022), the 1D CNN algorithm with the SA technique has not been investigated for damage classification of concrete anchorage zone. In this study, a 1-D CNN-based method is developed for autonomously classifying the damage feature in a concrete anchorage zone using the raw impedance signatures of the embedded SA sensor. Firstly, an overview of the developed method is presented. The fundamental theory of the SA technique is outlined, and a 1-D CNN classification model using the impedance signals is constructed. Secondly, the experiment on the SA-embedded concrete anchorage zone is carried out, and the impedance signals of the SA sensors are recorded under different applied force levels. Finally, the feasibility of the developed 1-D CNN model is examined for classifying concrete damage features with noise-contaminated signals

## 2. Methodology

### 2.1 Overview of method

The overview of a method for automated concrete damage classification is illustrated in Fig. 1. The key idea is to combine the smart aggregate-based impedance monitoring technique and the 1-D CNN-based damage classification model to classify concrete damage features induced by compression forces automatically. The proposed method combines feature extraction and damage classification tasks into a single architecture, enabling direct processing and automatic learning of optimal features from the raw impedance signals. This approach allows for streamlined and efficient analysis of the signal.

As shown in Fig. 1, the schematic of the proposed method includes two main stages: impedance

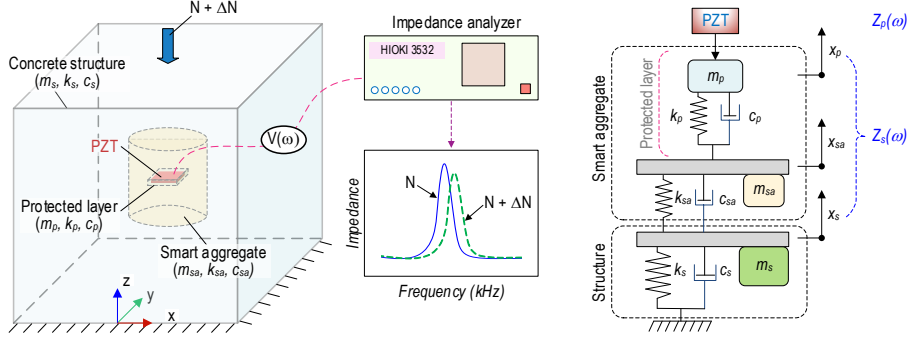


Fig. 2 Model of SA-based impedance monitoring for concrete structure

measurement (stage 1) and damage features classification (stage 2). The first stage consists of four steps: (1) to embed the smart aggregates (SA) on the target structure (i.e., concrete anchorage zone), (2) to excite the smart aggregates via a harmonic voltage in a high-frequency range, (3) to obtain raw impedance signals of the host structure under compression until failure using a wired impedance analyzer along with visual crack observation, and (4) to quantify the variations in measured impedance signals under loading cases and to define damage features by matching impedance signals variations, visual crack observation, and statistical indices (i.e., RMSD and CCD indices). The second stage includes three steps: (1) to generate training, validating, and testing datasets by adding noises to measured impedance signals, (2) to train a proposed 1-D CNN classification model, and (3) to predict the damage features by using the testing dataset.

## 2.2 Smart aggregate technique

Fig. 2 presents a model of smart aggregate-based impedance monitoring for concrete structures. The smart aggregate is fabricated by embedding a protected PZT sensor in a small concrete block. Then, the smart aggregate is installed in an inspected structure to obtain impedance signatures via the interaction between the PZT smart aggregate and the monitored structure. Note that the structural characteristics of the epoxy layer, the small concrete block, and the target structure would be changed corresponding to the variation of the applied force  $N$ .

The coupling motions of the coated layer, the concrete block, and the monitored structure could be demonstrated as a 3-degrees of freedom (3-DOF) impedance model (Huynh *et al.* 2020, Pham *et al.* 2021) (see Fig. 2(b)). The coupled structural-mechanical (SM) impedance  $Z_s$  of the protective layer, the concrete block, and the host structure can be presented as follows (Huynh *et al.* 2020, Pham *et al.* 2021)

$$Z_s = \frac{1}{j\omega} \left( K_{11} - \frac{K_{12}^2}{K_{11} + (K_{22} - K_{23}^2 / K_{33})} \right) \quad (1)$$

where the terms  $K_{mn}$  ( $m, n = 1-3$ ) are the dynamic stiffness components that depend on the structural features of the protective layer, the concrete block, and the host structure.

The electromechanical impedance  $Z(\omega)$  is computed using the SM impedance of the PZT sensor and that of the smart aggregate-host structure (Liang *et al.* 1994)

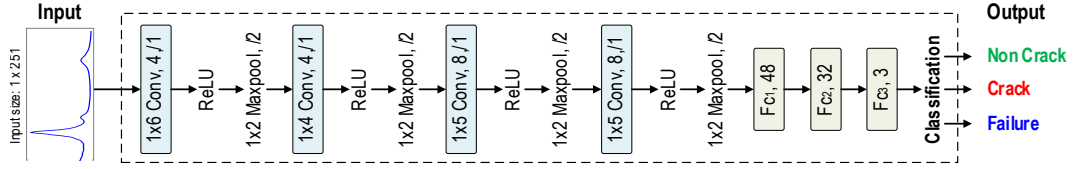


Fig. 3 The architecture of the 1-D CNN classification model using SA's raw impedance signals

Table 1 Specifications of 1-D CNN layers

No.	Type	Depth	Filter	Stride	No.	Type	Depth	Filter	Stride
1	Conv	4	1 x 6	1	9	Maxpool	-	1 x 2	2
2	ReLU	-	-	-	10	Conv	8	1 x 5	1
3	Maxpool	-	1 x 2	2	11	ReLU	-	-	-
4	Conv	4	1 x 4	1	12	Maxpool	-	1 x 2	2
5	ReLU	-	-	-	13	Fc <sub>1</sub>	48	-	-
6	Maxpool	-	1 x 2	2	14	Fc <sub>2</sub>	32	-	-
7	Conv	8	1 x 5	1	15	Fc <sub>3</sub>	3	-	-
8	ReLU	-	-	-	16	Classification	-	-	-

$$Z(\omega) = \left\{ j\omega \frac{w_p l_p}{t_p} \left[ \hat{\epsilon}_{33}^T - \frac{1}{Z_p(\omega)/Z_s(\omega) + 1} d_{31}^2 \hat{Y}_{11}^E \right] \right\}^{-1} \quad (2)$$

where  $w_p, l_p$  and  $t_p$  are the width, length, and thickness of the PZT patch, respectively;  $\hat{\epsilon}_{33}^T$  is the complex dielectric constant of at zero stress;  $Z_p(\omega) = \hat{Y}_{11}^E w_p t_p / (j\omega l_p)$  is the SM impedance of the PZT patch;  $d_{31}$  is the piezoelectric constant in one-direction at zero stress;  $\hat{Y}_{11}^E$  denotes the complex Young's modulus of PZT patch at the zero electric field.

### 2.3 1-D CNN classification model

Fig. 3 shows the architecture of the 1-D CNN classification model using SA's raw impedance signals. The model started with one Input layer, four Conv (Convolutional) layers, four ReLU (Rectified Linear Unit) layers, four Maxpool layers, three Fc (Fully Connected) layers, and finally, a Classification layer. The 1-D CNN model takes the  $1 \times 251$  series raw impedance signal as the input, then returns the output, which can be used for classifying damage features in the anchorage zone.

The detailed specifications of 1-D CNN layers are presented in Table 1. The Conv layer comprises a set of trainable filters or kernels that slide over each element of the input data. The filters multiply the corresponding entries of the filters and data and then add them up. Each filter generates a frame of the feature map in the next subsampling layer, and the depth of the convolution layer equals the number of frames. The ReLU layer replaces negative values from the output of the preceding layer with zero while keeping all positive values. The Maxpool layer slides filters over the output of the preceding layer and extracts the element with the highest value. The purpose of the

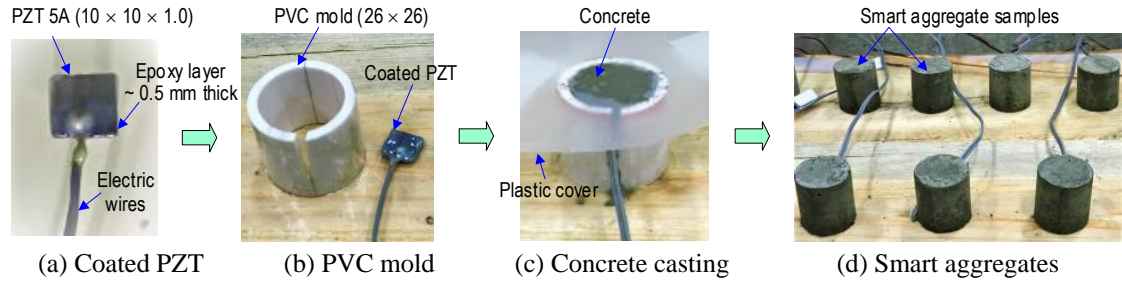


Fig. 4 Fabrication of smart aggregate

Table 2 Concrete components for the anchorage zone\*

Material for 1 m <sup>3</sup>	Mass (kg)
Sand	800
Coarse aggregate ( $D_{\max}$ 25)	997
Cement	346
Water (liter)	165

(\*) SA was constructed using the same components of the anchorage zone without coarse aggregate

Maxpool layer is to reduce the computational cost by decreasing the size of the convolved feature. The Fc layers establish all possible connections between layers, meaning every input from the preceding layer influences every element of the output layer. The Fc layers combine and transform learned features into lower-dimensional representations suitable for the Classification layer.

### 3. Experiment

#### 3.1 Fabrication of smart aggregate

Fig. 4 shows the fabrication of the smart aggregate, which was used to monitor the structural health of a concrete anchorage zone, in the next section, Section 3.2. The PZT 5A patch ( $10 \times 10 \times 1$  mm) was joined with electric wires to form a PZT sensor for impedance measuring. The sensor was protected by an epoxy layer around 0.5 mm thickness (see Fig. 4(a)). A PVC mold, which had a height of 26 mm and an inner diameter of 26 mm, was prepared for concrete casting (see Fig. 4(b)). After that, the coated PZT sensor was embedded in the center of the mold during concrete casting to form a smart aggregate sensor (see Fig. 4(c)). The concrete mixture used for the monitored structures (i.e., the concrete anchorage zone), including cement, sand, and water (without coarse aggregates), was employed for the SA's construction (see Table 2). The smart aggregate was removed from the mold after 24 hours of casting. Then, it was cured using a wet blanket for 28 days before installing it in the anchorage zone for impedance monitoring. The smart aggregate samples are shown in Fig. 4(d). The material properties of the components for the smart aggregate are listed in Table 3.

Table 3 Material properties of components for smart aggregate

Properties	PZT 5A	Epoxy Layer	Concrete
Mass density, $\rho$ (kg/m <sup>3</sup> )	7750	1090	2300
Young's modulus, $E$ (GPa)	62.1	0.74	23.6
Poisson's ratio, $\nu$	0.35	0.3	0.2
Compressive strength, $\sigma_c$ (MPa)		32.3	23.3*
Damping loss factor, $\eta$	0.0125		
Dielectric constant, $\epsilon_{33}^T$ (F/m)	$1.53 \times 10^{-8}$		
Coupling constant, $d_{31}$ (m/V)	$-1.71 \times 10^{-10}$		
Dielectric loss factor, $\delta$	0.015		

(\*) Compressive strength was determined by a uniaxial compressive test on a standard concrete cylinder (150 × 300 mm)

### 3.2 Experimental setup for impedance monitoring of anchorage zone under compression

#### 3.2.1 Experimental setup

Fig. 5 shows the schematic of an experiment on a lab-scale concrete anchorage zone embedded with smart aggregates under compression (Pham *et al.* 2021). The experiment was performed to obtain impedance responses of smart aggregates under the loading process. These impedance signals will be employed for data generation and fed to the 1-D CNN classification model. The anchorage zone consists of a Polyvinyl chloride (PVC) cylinder, a pure concrete block, and four steel blocks. The PVC cylinder played a role as a duct for passing the prestressing strands (see Fig. 5(a)). Four steel blocks were uniformly spread on the concrete surface, and their distance to the center of the anchorage zone was 65 mm (see Figs. 5(a) and 5(b)). These blocks were used as a bearing plate (Vsl 2018) to transfer the prestress forces to the structure. The material properties of the concrete are detailed in Table 3.

For impedance monitoring, two smart aggregate sensors described in Section 3.1, namely SA1 and SA2, were installed in the concrete anchorage zone (see Figs. 5(a) and 5(b)) (Pham *et al.* 2021). The distance between the centers of these SA sensors to the concrete surface was set at about 35 mm. Note that SA1 was embedded in the left side of the anchorage zone, and SA2 was embedded in the right one. For the compression test, the anchorage zone was put on a supporting steel frame, which included two thick steel plates connected using four steel tubes and bolt connections (see Fig. 5(a)) (Pham *et al.* 2021). The steel frame was designed to resist tension induced by the anchorage zone. The compression force was generated via a hydraulic jack, and a combination of a load cell and indicator was utilized to monitor the actual compressive forces.

#### 3.2.2 Loading cases and visual crack observation

As listed in Table 4, eleven loading cases were assigned for impedance measurement in the anchorage zone. The compressive force P1 was set as the baseline at 100 kN, and the forces were gradually increased for the first six loading cases (P1-P6) from 100 to 200 kN with an increment of

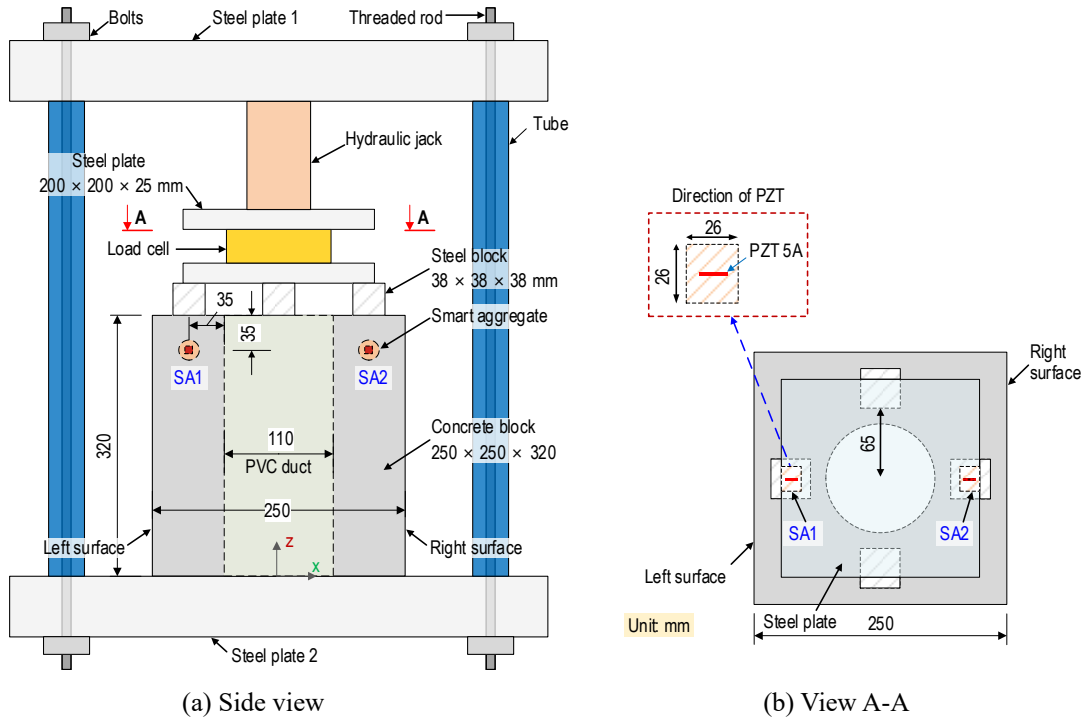


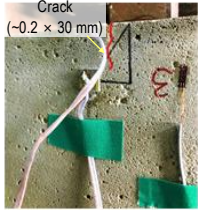
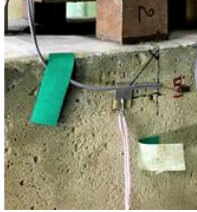
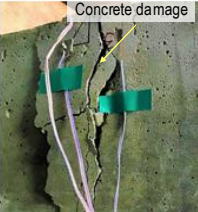
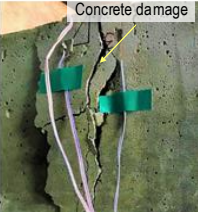
Fig. 5 Schematic of the testing setup of impedance monitoring for anchorage zone under compression

20 kN. The applied forces were then raised from 200 to 230 kN for the next three loading scenarios (P7-P9) with an interval of 10 kN. Following that, during the P10 loading case, the compression force was increased to 235 kN, resulting in a partial collapse of the concrete. Finally, the applied force decreased to P11, set at 102 kN.

As described in Table 4, the bearing stress  $\sigma_{be}$  ranged from 17.3-40.7 MPa (i.e., 0.74-1.74 $\sigma_c$ ) under the compression forces P1-P11. The bearing stress in the anchorage zone with reinforcement allows from 1.25 to 3.0 $\sigma_{ci}$ , in which  $\sigma_{ci}$  is the compressive strength of the concrete at the installation of the steel strands. As observed during the experiment, the concrete crack occurred on the left surface (near SA1) under the bearing stress  $\sigma_{be} = 1.71\sigma_c$  (i.e., under the loading case P9), and the concrete collapsed under  $\sigma_{be} = 1.74\sigma_c$  (under force P10). The visual crack observation during the loading procedure is detailed in Table 4. There was no crack when the applied force was lower than P8 = 220 kN. A pristine crack was detected on the left surface of the anchorage zone (near SA1) under the loading case P9 = 230 kN. Then, the crack propagated, and the concrete collapsed first on the left side close to SA1. After that, larger cracks appeared on the right side (close to SA2), leading to concrete failure.

The impedance signals of the smart aggregates were measured using a wired impedance analyzer, specifically the HIOKI 3532. The analyzer excited a harmonic voltage of 1 V and recorded the impedance signals of the smart aggregates within a frequency range of 100-600 kHz (251 points). For each loading case, impedance signals were obtained four times or four ensembles. The laboratory temperature was kept constant at approximately 22°C during the monitoring process to minimize the influence of temperature changes on the impedance responses.

Table 4 Applied loading history and crack observation on the anchorage zone (Pham *et al.* 2021)

Case	Applied force		Observation of crack development on concrete surface	
	P (kN)	Bearing stress $\sigma_{be}$ (MPa)*	On the left surface (near SA1)	On the right surface (near SA2)
P1→ P6	100 → 200 (20 kN increment)	17.3 → 34.6 (3.47 MPa increment)	No crack occurrence	No crack occurrence
P7	210	36.4		
P8	220	38.1		
P9	230	39.8	Initiation of surface crack 	No crack occurrence 
P10	235	40.7	Cracks propagation and concrete failure 	Large crack occurrence and concrete failure 
P11	102	17.7		

(\*) Stress ahead of steel blocks (bearing plate) is so-called bearing stress

### 3.3 Impedance signal of smart aggregates

Fig. 6 shows the impedance signals of SA1 under loading cases P1-P11, which were used to feed to the 1-D CNN classification model. It can be noted that the impedance signals are more sensitive to the applied forces at the highest peaks around 210 kHz. The impedance signatures of SA1 were slightly changed under forces P1-P6. Then a sudden change occurred under force P7, thus showing a transformation of the concrete domain surrounding SA1 (e.g., inner concrete damage (Kocherla *et al.* 2020)). The signals were constantly varied under force P8, and another abrupt variation appeared under loading case P9 (the pristine crack close to SA1). The impedance signatures changed under force P10 (crack propagation), and the most variation in signals of SA1 occurred under force P11 (concrete failure). The impedance signatures of SA1 were matched to the crack appearances to make the following observations. First, when cracks occurred, significant changes in impedance signals were observed in SA1. Second, early incipient cracks and concrete

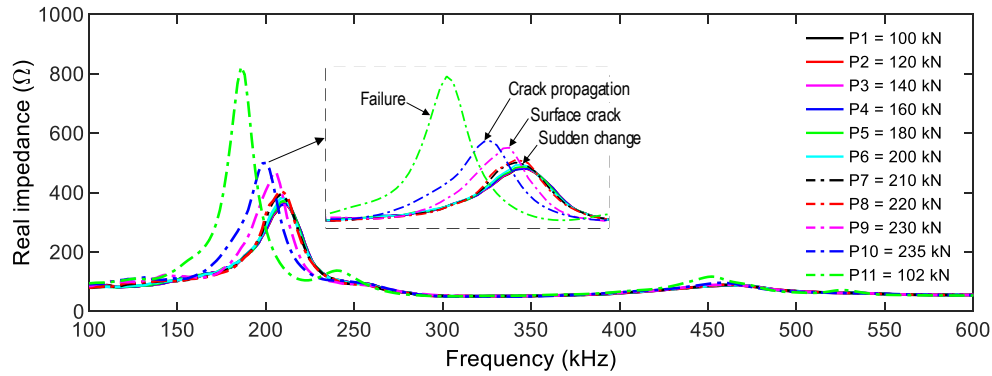


Fig. 6 Real impedance signals of SA1 under compression forces

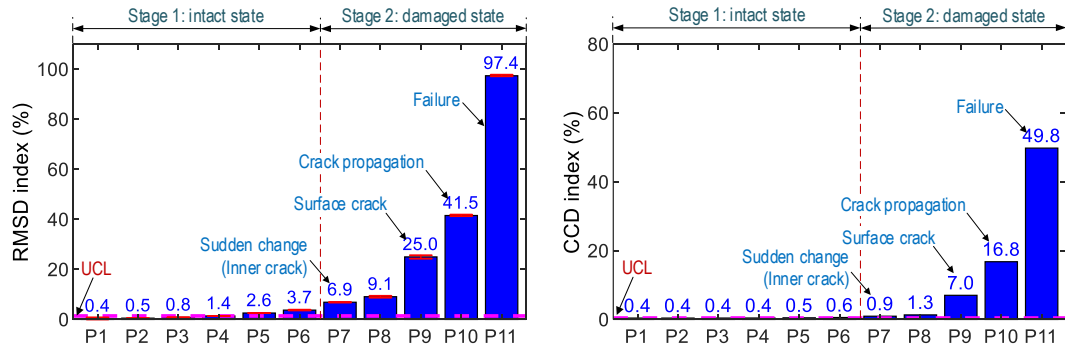


Fig. 7 RMSD and CCD indices quantified from variations in real impedance signals of SA1

damage appeared on the anchorage zone's left side, possibly due to unequally applied force (via four steel blocks) and the concrete structure's inelastic nature.

To quantify the change in the SA's impedance signatures, the RMSD index (Sun *et al.* 1995, Huynh *et al.* 2014) and the CCD index (Zagrai and Giurgiutiu 2002, Huynh *et al.* 2014) are utilized. Furthermore, the upper control limit (UCL) control threshold was established to aid decision-making (Huynh *et al.* 2014). The error bars, which represent the standard deviation of the impedance signatures obtained from the four ensembles, are also presented. Fig. 7(a) displays the RMSD indices obtained from the variations in impedance signals of the smart aggregates SA1 within the 100-600 kHz frequency range. The RMSD values were negligible (0.4%) in the intact state and increased gradually under loading conditions. The small standard deviations of the impedance signals, as indicated by the error bars, suggest that the impedance signals are stable. The RMSD indices for forces P1-P6 (0.4–3.7%) were insignificant in SA1 (see Fig. 7(a)). However, when force P7 was applied, the RMSD index (6.9%) became significant (about twice as large as that under P6), suggesting sudden changes in the concrete surrounding SA1. The RMSD index (25%) under P9 was about three times that under force P8, potentially caused by inner damage that instigated the incipient surface crack. The maximum RMSD value (97.4%) was observed under force P11.

Fig. 7(b) presents the CCD indices computed from the changes in impedance signals of SA1 within the measured frequency range. The CCD values were insignificant (0.4%) in the intact state

and increased gradually during loading. As the error bars indicate, the slight standard deviations of the impedance signals suggest less dispersion in impedance signals. The CCD indices for forces P1-P6 (0.4–0.6%) were insignificant in SA1 (see Fig. 7(b)). However, when force P7 was applied, the CCD value (0.9%) became significant, suggesting sudden alterations in the concrete surrounding SA1. The CCD index (7%) under force P9 was about five times that under force P8, potentially caused by inner damage that caused the incipient surface crack. The maximum CCD value (49.8%) was observed under force P11 (concrete failure). RMSD and CCD analyzed indices confirmed that the variations in impedance signatures of the PZT-embedded smart aggregate were induced by concrete damage.

## 4. Damage classification results

### 4.1 Databank generation

The signals of SA1, which were measured for eleven force levels (i.e., P1-P11), were used to construct the databank for the 1-D CNN model. The noise was injected considering the uncertainty of the measurement situation under the premise that the measured impedance signal data is insufficient for deep learning training, validation, and testing. The noise was injected into the impedance signal using Gaussian noise with several signal-to-noise ratio (SNR) levels. The following formula calculates the SNR level in decibels (dB) (Johnson 2006).

$$SNR = 10 \log_{10} \left( \frac{P^{signal}}{P^{noise}} \right) \quad (3)$$

As shown in Fig. 8, the combination of measured signals and generated signals with SNRs of 35 dB and 30 dB formed the training and validation datasets. Those datasets were used to train and validate the 1-D CNN model. The performance of the trained model in classifying damage features was evaluated by the testing datasets, which were generated impedance signals with SNRs ranging from 20 dB to 16 dB with an interval of 2 dB.

Since 1-D CNN models require data and corresponding annotated labels to train, a process called data labeling is needed. This process is to form a representation of what class of data signals belong to. Table 5 shows the structural observed status near the SA1 sensor during the experiment's loading of the eleven cases (i.e., P1-P11). Each observed status is assigned and grouped under the three labels "Non Crack", "Crack", and "Failure". The "Non Crack" label includes force cases ranging from P1 to P5, corresponding with the observed status "No crack". The "Crack" label includes force cases ranging from P6 to P10, which correspond to the observed status "Inner crack", "Inner crack + surface crack + crack propagation", and "Crack propagation". The "Failure" label is used for force case P11 corresponding to the observed status "Failure". Fig. 9 shows the impedance signals classified under these assigned labels.

The 1-D CNN model requires a massive dataset for training and validation to achieve a reasonable generalization capability. In the experiment, the impedance signals of SA1 were recorded with four ensembles for each force case. Three groups, "Non Crack" (for P1-P5), "Crack" (for P6-P10), and "Failure" (for P11), have 20, 20, and 4 impedance signals, respectively. Table 6 shows the training and validating data for the 1-D CNN model. As mentioned in Fig. 8 and shown in this table, impedance signals having noise SNRs of 35 dB and 30 dB were generated to overcome the limitation

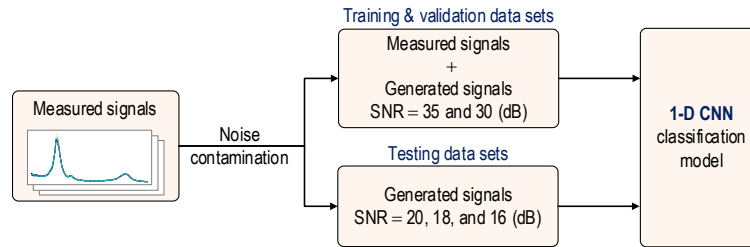


Fig. 8 Workflow of data generation for training and testing 1-D CNN model

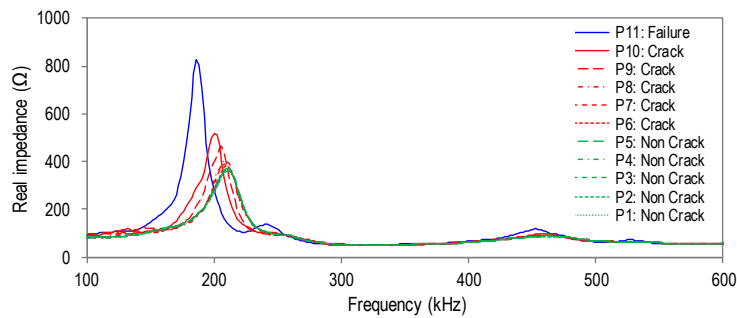


Fig. 9 Impedance signals classified under three assigned labels

Table 5 Assigned lab

Force case	Observed status	Assigned label
P1	No crack	Non Crack
P2	No crack	
P3	No crack	
P4	No crack	
P5	No crack	
P6	Inner crack	Crack
P7	Inner crack	
P8	Inner crack	
P9	Inner crack + surface crack + crack propagation	
P10	Crack propagation	Failure
P11	Failure	

in the amount of actually measured impedance signal data. With each SNR level, 20, 20, and 18 impedance signals were generated in three groups "Non Crack," "Crack", and "Failure", respectively. Thus, a total of 160 samples were collected from the measured signals and the noise-contaminated generated signals. 80% of the total samples were used for training, and 20% were used for validating the 1-D CNN model. The number of signals is chosen to prevent the bias phenomenon of assigned class labels (Tyagi and Mittal 2020) in training the proposed model.

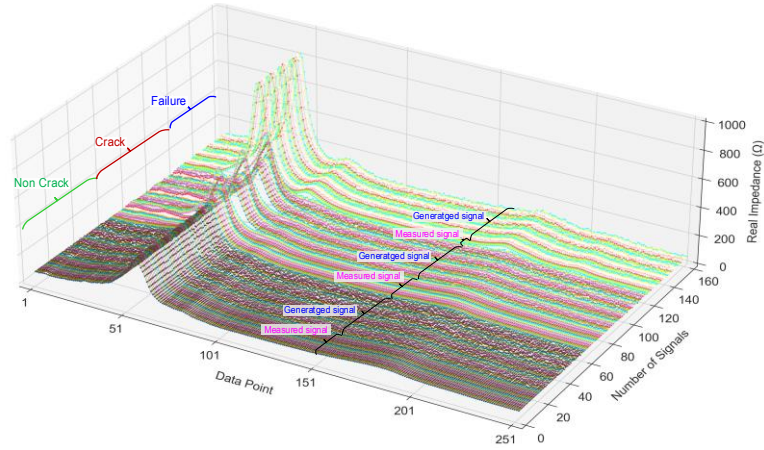


Fig. 10 3-D visualization of impedance dataset for three assigned labels

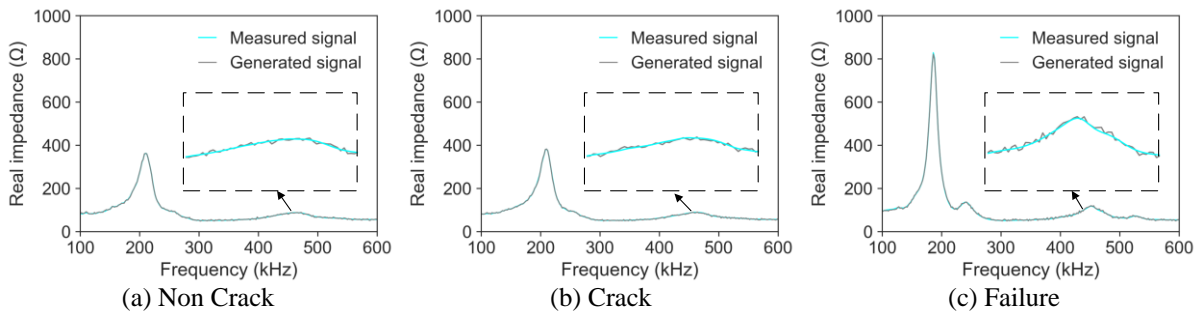


Fig. 11 Adding noise to impedance signal with SNR = 35 (dB)

In Fig. 10, the whole impedance dataset belonging to three assigned labels (i.e., "Non Crack", "Crack", "Failure") for training and validating the 1-D CNN model is visualized in 3-D (three-dimensional) format. There were 160 impedance signals (i.e., measured and generated signals) from eleven force cases (i.e., P1-P11). Each impedance signal was recorded at 251 data points of real impedance values corresponding to applied force levels. As a result, a total of 40160 data points were recorded and divided into three groups "Non Crack", "Crack", and "Failure", with 15060, 15060, and 10040 data points, respectively. Several changes in the magnitude of generated signals caused by noises can be visually recognized when compared to the measured signals.

Figs. 11 and 12 illustrate examples of adding different noises to impedance signals belonging to three assigned labels. We generated noise injection signals with SNRs of 35 and 30 dB at 251 measurement points for each signal sample. With the same measured impedance signals, the larger the SNR, the smaller the noise is added. As a result, the impedance signal changes when adding noise with an SNR of 35 dB are smaller than that of 30 dB. It can be seen that noise with SNRs of 35 dB and 30 dB induces an insignificant effect on the general shape of the measured signals while it can simulate the realistic situations of noise contamination.

To construct testing datasets, the measured signals were injected by different SNR levels ranging from 20 to 16 dB with an interval of 2 dB. Adding such noises to signals could help to test the

Table 6 Training and validating data

Assigned label	Current sample	Generated sample via SNR		Total sample	Ratio (Train/Validation)
		35 (dB)	30 (dB)		
Non Crack	20	20	20	60	80/20
Crack	20	20	20	60	
Failure	4	18	18	40	

Table 7 Number of testing data sets for evaluating trained model

Assigned label	Generated sample via SNR		
	20 (dB)	18 (dB)	16 (dB)
Non Crack	60	60	60
Crack	60	60	60
Failure	40	40	40

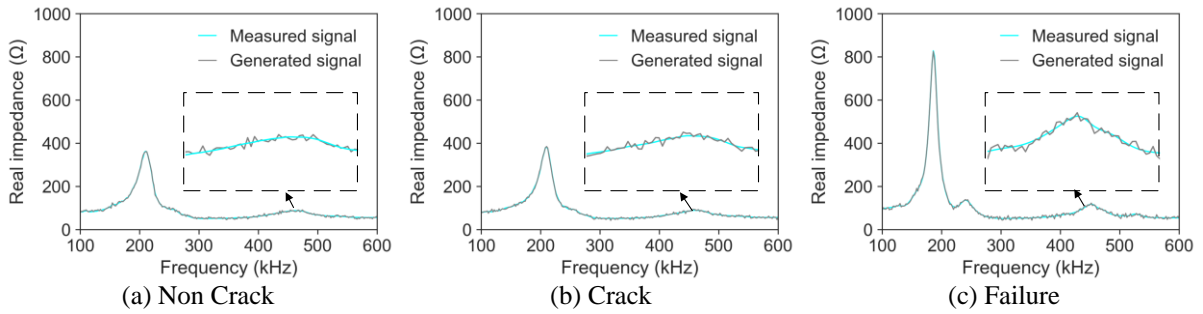


Fig. 12 Adding noise to impedance signal with SNR = 30 (dB)

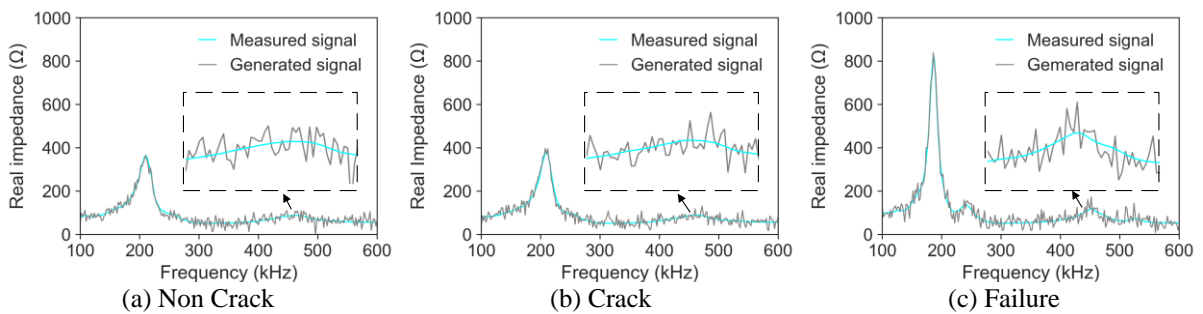


Fig. 13 Adding noise to impedance signal with SNR = 16 (dB)

reliability and generalization of the 1-D CNN model on unseen testing data. As shown in Table 7, in each noise level, there were 60, 60, and 40 new signals were generated in three groups "Non Crack", "Crack", and "Failure", respectively. A total of 480 signals were utilized for testing the 1-D

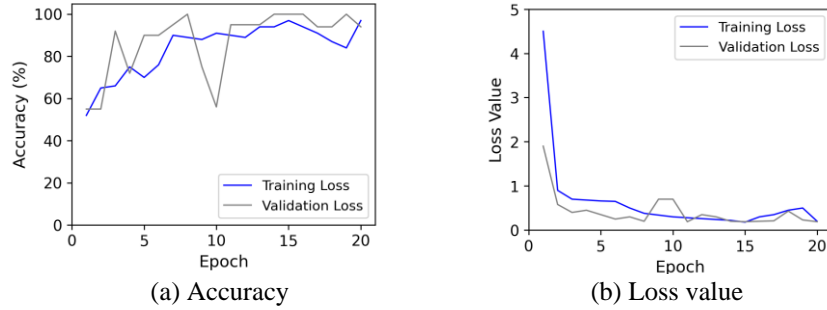


Fig. 14 Accuracy and loss value during training and validating

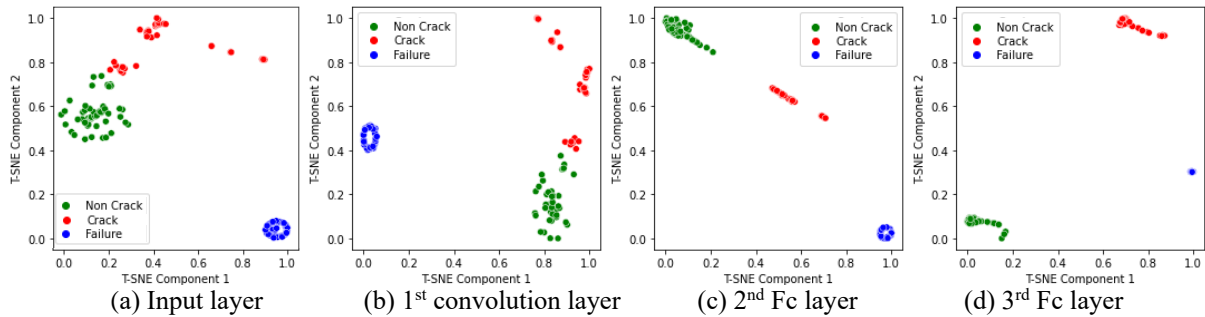


Fig. 15 Feature visualization of training data after each layer via using the t-SNE algorithm

CNN model. The noise-contaminated signals in three groups corresponding to SNR of 16 dB are illustrated in Figs. 13.

#### 4.2 Training and validation results

All experiments were performed on a desktop computer (GPU: GTX 2080 Ti 11G, CPU: Intel i9-9000KF 3.6 GHz, RAM: 64 GB). The 1-D CNN model was programmed using Python programming language (version 3.8). The designed 1-D CNN model was trained using the Adam training algorithm (Kingma and Ba 2014) with a mini-batch size of 1 and a learning rate of 0.001.

Fig. 14 shows the accuracy and loss value during the training and validation process of the 1-D CNN model. The training and validation accuracy of the 1-D CNN model gradually increased and reached over 95% at the 20<sup>th</sup> epoch. At the same time, the training and validation losses sharply reduce in a few first epochs and continue to converge at the end of the learning process. At the 20<sup>th</sup> epoch, the training and validation losses are recorded at approximately 0.1, suggesting the high accuracy of the trained 1-D CNN model.

Fig. 15 visualizes the characteristics of impedance data passed through each layer of the 1-D CNN during the learning process using the t-distributed stochastic neighbor embedding (t-SNE) algorithm (Van Der Maaten and Hinton 2008). The t-SNE algorithm can project a high-dimensional convolution layer space into a low-dimensional space while preserving local structure. This means that points located close together in the high-dimension dataset tend to locate close together in the chart. In the Input layer, the positions of impedance signals, which are classified into three groups,

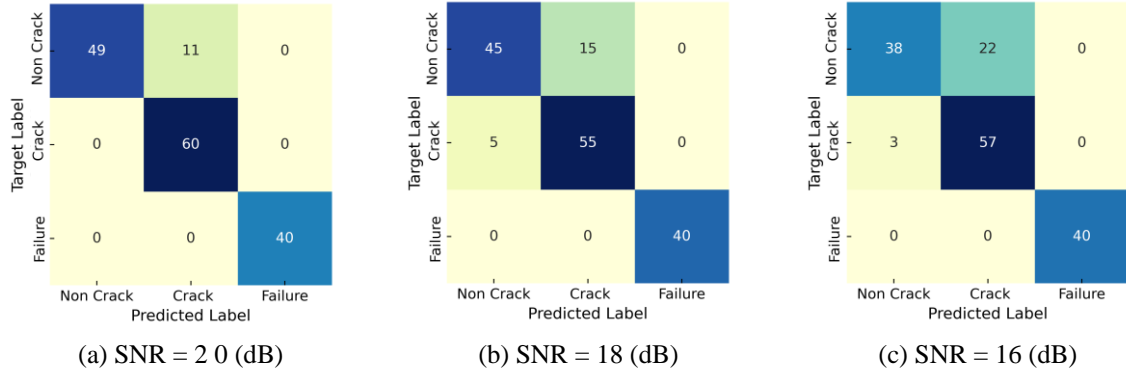


Fig. 16 Confusion matrix

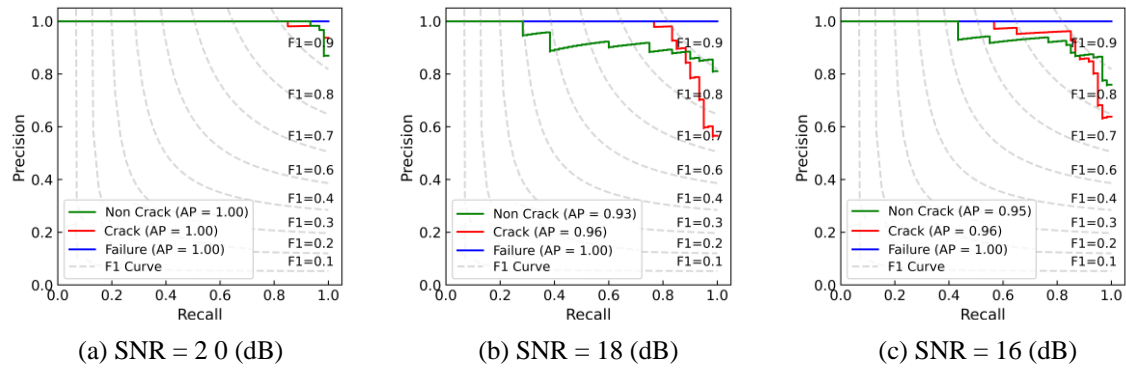


Fig. 17 P-R curve and F1 curve

"Failure", "Crack", and "Non Crack", form three clusters. Through training layers, it can be seen that the impedance signals among one group tend to move closer together while the distances among groups become larger. As shown in Fig. 15(d), the characteristics of the three groups in the third Fc layer can be easily classified. As a result, the proposed 1-D CNN model can learn and classify damage features from impedance signals.

#### 4.3 Performance under Noise Levels

Fig. 16 illustrates the results of the damage feature classification of the trained model utilizing confusion matrixes without normalization. The confusion matrixes were plotted to show the number of correctly classified signals reflected in Table 7. Using absolute values in the confusion matrix to highlight correct classifications of investigated sample numbers has been utilized in some previous research studies (Mei *et al.* 2020, Yang *et al.* 2022). As shown in this figure, in each SNR level, a total of 160 data samples in testing datasets are used to evaluate the performance of the model. With the SNR value of 20 dB, there are 11 samples that are misclassified between "Crack" and "Non Crack" conditions. The misclassified samples increased to 20 and 25, corresponding to SNR levels

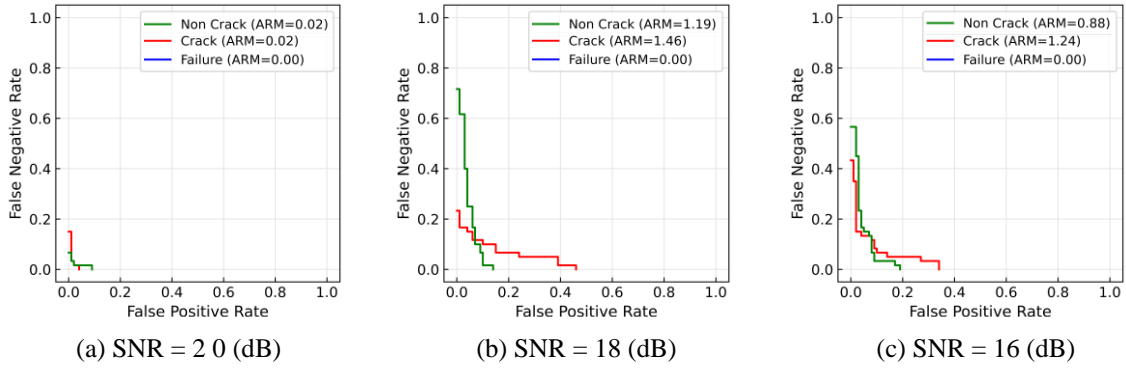


Fig. 18 Relationship between false positive and false negative

of 18 and 16 dB, respectively. It can be concluded that as the SNR level decreases, the accuracy of prediction labels tends to decrease.

As evaluation indicators, precision, recall, false negative rate, and false positive rate, which are calculated from four basic evaluation factors: true positive, true negative, false positive, and false negative, are applied. Fig. 17 illustrates the performance of the trained 1-D CNN classification model, which is evaluated using precision/recall (P-R) and fusion (F1) curves. Higher precision means that the 1-D CNN model returns more relevant results than irrelevant ones, and high recall means that the 1-D CNN model returns most of the relevant results. The integration of the area under the P-R curve is called average precision (AP) and indicates the classification ability of the 1-D CNN model. The F1 curve measured the similarity between the predicted and target labels. In Fig. 17, the AP indices reached 1.00, and the F1 score was larger than 0.9 in all three groups, indicating the high accuracy and reliability of the detector at SNR = 20 dB. In Figs. 17(b) and 17(c), when decreasing the SNR, the results show that the 1-D CNN maintained its classification performance as the AP indices are larger than 0.90.

Fig. 18 analyses the prediction accuracy of the 1-D CNN classification model as the relationship between false positive and false negative rates. The integration of the area under the curve is called the average miss rate (AMR), and the lower the AMR value, the better the performance of the 1-D CNN model is (Huynh 2021). As shown in Fig. 18(a), the AMR indicated that classification had the highest accuracy at SNR = 20 dB as the AMR of the "Failure" label is 0, and the AMR of the "Crack" and "Non Crack" labels are both 0.02. In Figs. 18(b) and 18(c), the AMR value of the "Failure" label is maintained at 0, while the AMR of the "Crack" and "Non Crack" increased. It is indicated that the classification accuracy of the 1-D CNN decreases when the SNR decreases. The reduction in classification accuracy comes from the misclassification between "Crack" and "Non Crack" labels.

## 5. Conclusions

In this study, the 1-D CNN-based method was developed for autonomously classifying the damage feature in the concrete anchorage zone using the raw impedance signatures of the embedded SA sensor. Firstly, the overview of the developed method was presented. The fundamental theory of the SA technique was outlined, and the 1-D CNN classification model learned the impedance

signals for classifying the damage feature induced by compression was constructed. Secondly, the compression experiment on the SA-embedded concrete anchorage zone was carried out, and the impedance signals of the SA sensors were recorded under different applied force levels. Finally, the feasibility of the developed 1-D CNN model for classifying concrete damage features with noise-contaminated signals was examined. The results revealed that the developed method could accurately classify the damaged features in the concrete anchorage zone.

Based on the analyzed results, the following remarks could be drawn: (1) the proposed classification model implicitly processes the raw impedance signals obtained from smart aggregates and autonomously outputs the concrete damage features; (2) the accuracy of the 1-D CNN model was significantly influenced by noises in the impedance signal, and the classification accuracy decreased with the increased of noise level; (3) the proposed 1-D CNN model was able to classify damage features even if from impedance signals having contaminated noises larger than noises in impedance signals used to train the model.

Although the developed 1-D CNN architecture could show promising performance in classifying damage features in concrete anchorage zone, its backbone was still simple and have not been extensively studied yet. Therefore, the future study remains: (1) to classify other observed damage features (e.g., inner damage propagation) by extending outputs for the proposed model and labeling the relevant data in the gathered dataset, (2) to improve the accuracy of the model by optimizing the model parameters (e.g., layers, hyper-parameters, etc.). Additionally, damage in the concrete anchorage zone may occur in several locations when conducting compression experiments. Hence, re-constructing the current model for extracting multi-damage features using several SA sensors impedance responses should be implemented to accurately identify local damage positions in concrete anchorage structures.

### Author contributions

Quoc-Bao Ta, Quang-Quang Pham, and Jeong-Tae Kim developed the methodology; Quang-Quang Pham and Quoc-Bao Ta conducted the experiment for data collection; Quoc-Bao Ta performed the framework design and simulation for the 1-D CNN model; Quoc-Bao Ta, Quang-Quang Pham, and Ngoc-Lan Pham designed the logic of the manuscript; Quoc-Bao Ta, Quang-Quang Pham, and Ngoc-Lan Pham wrote the manuscript; Jeong-Tae Kim revised the manuscript and supervised the whole work. All authors have read and agreed to the submitted version of the manuscript.

### Acknowledgments

This work was supported by a Research Grant from Pukyong National University (2021-2023).

### References

- Abdeljaber, O., Avci, O., Kiranyaz, M.S., Boashash, B., Sodano, H. and Inman, D.J. (2018), "1-D CNNs for structural damage detection: Verification on a structural health monitoring benchmark data", *Neurocomput.*, **275**, 1308-1317. <https://doi.org/10.1016/j.neucom.2017.09.069>.

- Ai, D., Luo, H. and Zhu, H. (2019), "Numerical and experimental investigation of flexural performance on prestressed concrete structures using electromechanical admittance", *Mech. Syst. Signal Pr.*, **128**, 244-265. <https://doi.org/10.1016/j.ymsp.2019.03.046>.
- Ai, D., Mo, F., Han, Y. and Wen, J. (2022), "Automated identification of compressive stress and damage in concrete specimen using convolutional neural network learned electromechanical admittance", *Eng. Struct.*, **259**, 114176. <https://doi.org/10.1016/j.engstruct.2022.114176>.
- Aryan, P., Sampath, S. and Sohn, H. (2018), "An overview of non-destructive testing methods for integrated circuit packaging inspection", *Sensors*, **18**(7), 1981. <https://doi.org/10.3390/s18071981>.
- Cancelli, A., Laflamme, S., Alipour, A., Sritharan, S. and Ubertini, F. (2019), "Vibration-based damage localization and quantification in a pretensioned concrete girder using stochastic subspace identification and particle swarm model updating", *Struct. Health Monit.*, **19**(2), 587-605. <https://doi.org/10.1177/1475921718820015>.
- Gu, H., Song, G., Dhonde, H., Mo, Y.L. and Yan, S., (2006), "Concrete early-age strength monitoring using embedded piezoelectric transducers", *Smart Mater. Struct.*, **15**(6), 1837. <https://doi.org/10.1088/0964-1726/15/6/038>.
- Ho, D.D., Kim, J.T., Stubbs, N. and Park, W.S. (2012), "Prestress-force estimation in PSC girder using modal parameters and system identification", *Adv. Struct. Eng.*, **15**(6), 997-1012. <https://doi.org/10.1260/1369-4332.15.6.997>.
- Hou, D.W., Zhao, J.L., Shen, J.S.L. and Chen, J. (2017), "Investigation and improvement of strut-and-tie model for design of end anchorage zone in post-tensioned concrete structure", *Constr. Build. Mater.*, **136**, 482-494. <https://doi.org/10.1016/j.conbuildmat.2017.01.033>.
- Huynh, T.-C., and Kim, J.-T. (2014), "Impedance-based cable force monitoring in tendon-anchorage using portable pzt-interface technique", *Math. Probl. Eng.*, **2014**, 1-11. <https://doi.org/10.1155/2014/784731>
- Huynh, T.C., (2021), "Vision-based autonomous bolt-looseness detection method for splice connections: Design, lab-scale evaluation, and field application", *Automat. Constr.*, **124**, 103591. <https://doi.org/10.1016/j.autcon.2021.103591>
- Huynh, T.C., Nguyen, T.D., Ho, D.D., Dang, N.L. and Kim, J.T. (2020), "Sensor fault diagnosis for impedance monitoring using a piezoelectric-based smart interface technique", *Sensors*, **20**(2), 510. <https://doi.org/10.3390/s20020510>.
- Johnson, D.H. (2006), "Signal-to-noise ratio", *Scholarpedia*, **1**(12), 2088. <https://doi.org/10.4249/scholarpedia.2088>.
- Kingma, D.P. and Ba, J., (2014) "Adam: A method for stochastic optimization", arXiv preprint arXiv:1412.6980. <https://doi.org/10.48550/arXiv.1412.6980>.
- Kocherla, A. and Subramaniam, K.V.L. (2020), "Embedded smart PZT-based sensor for internal damage detection in concrete under applied compression", *Measurement*, **163**, 108018. <https://doi.org/10.1016/j.measurement.2020.108018>.
- Lee, S., Kalos, N. and Shin, D.H. (2014), "Non-destructive testing methods in the US for bridge inspection and maintenance", *KSCE J. Civ. Eng.*, **18**(5), 1322-1331. <https://doi.org/10.1007/s12205-014-0633-9>.
- Liang, C., Sun, FP, and Rogers, C.A. (1994), "Coupled electromechanical analysis of adaptive material systems-determination of the actuator power consumption and system energy transfer", *J. Intell. Mater. Syst. Struct.*, **8**(4), 335-343. <https://doi.org/10.1177/1045389X9700800406>.
- Mehrabi, A.B., Ligozio, C.A., Ciolko, A.T. and Wyatt, S.T. (2010), "Evaluation, rehabilitation planning, and stay-cable replacement design for the hale boggs bridge in Luling, Louisiana", *J. Bridge Eng.*, **15**(4), 364-372. [https://doi.org/10.1061/\(ASCE\)BE.1943-5592.0000061](https://doi.org/10.1061/(ASCE)BE.1943-5592.0000061).
- Mei, Z., Ivanov, K., Zhao, G., Wu, Y., Liu, M. and Wang, L. (2020), "Foot type classification using sensor-enabled footwear and 1D-CNN", *Measurement*, **165**, 108184. <https://doi.org/10.1016/j.measurement.2020.108184>.
- Min, J., Park, S. and Yun, C.B. (2010), "Impedance-based structural health monitoring using neural networks for autonomous frequency range selection", *Smart Mater. Struct.*, **19**(12), 125011. <https://doi.org/10.1088/0964-1726/19/12/125011>.
- Na, W.S. and Baek, J. (2018), "A review of the piezoelectric electromechanical impedance based structural

- health monitoring technique for engineering structures”, *Sensors*, **18**(5), 1307. <https://doi.org/10.3390/s18051307>.
- Nguyen, T.T., Ta, Q.B., Ho, D.D., Kim, J.T. and Huynh, T.C. (2021), “Deep learning-based functional assessment of piezoelectric-based smart interface under various degradations”, *Smart Struct. Syst.*, **28**(1), 69-87. <https://doi.org/10.12989/sss.2021.28.1.069>.
- Nguyen, T.T., Tuong Vy Phan, T., Ho, D.D., Man Singh Pradhan, A. and Huynh, T.C. (2022), “Deep learning-based autonomous damage-sensitive feature extraction for impedance-based prestress monitoring”, *Eng. Struct.*, **259**, 114172. <https://doi.org/10.1016/j.engstruct.2022.114172>.
- Park, G., Sohn, H., Farrar, C.R. and Inman, D.J. (2003), “Overview of piezoelectric impedance-based health monitoring and path forward”, *Shock Vib. Dig.*, **35**(6), 451-464. <https://doi.org/10.1177/05831024030356001>.
- Pham, Q.Q., Dang, N.L. and Kim, J.T. (2021), “Piezoelectric sensor-embedded smart rock for damage monitoring in a prestressed anchorage zone”, *Sensors*, **21**(2), 353. <https://doi.org/10.3390/s21020353>.
- Sony, S., Dunphy, K., Sadhu, A. and Capretz, M. (2021), “A systematic review of convolutional neural network-based structural condition assessment techniques”, *Eng. Struct.*, **226**, 111347. <https://doi.org/10.1016/j.engstruct.2020.111347>.
- Sun, F.P., Chaudhry, Z., Liang, C. and Rogers, C.A. (1995), “Truss structure integrity identification using pzt sensor-actuator”, *J. Intell. Mater. Syst. Struct.*, **6**(1), 134-139. <https://doi.org/10.1177/1045389X9500600117>.
- Tyagi, S. and Mittal, S. (2020), “Sampling approaches for imbalanced data classification problem in machine learning”, *Proceedings of the ICRIC 2019: Recent Innovations in Computing*, Springer International Publishing. [https://doi.org/10.1007/978-3-030-29407-6\\_17](https://doi.org/10.1007/978-3-030-29407-6_17).
- Van Der Maaten, L. and Hinton, G.J.J.O.M.L.R. (2008), “Visualizing data using t-SNE”, *J. Mach. Learn. Res.*, **9**(86), 2579-2605.
- Vsl (2018), VSL Strand Post-Tensioning Systems. Available online: <https://vsl.com/home/technologies/post-tensioning-systems/> (accessed on 6 January 2022).
- Wu, C., Xiang, H., Jiang, S. and Ma, S. (2022), “Stress monitoring of concrete via uniaxial piezoelectric sensor”, *Sensors*, **22**(11), 4041. <https://doi.org/10.3390/s22114041>.
- Wu, T., Liu, G., Fu, S. and Xing, F. (2020), “Recent progress of fiber-optic sensors for the structural health monitoring of civil infrastructure”, *Sensors*, **20**(16), 4517. <https://doi.org/10.3390/s20164517>.
- Yang, Z., Gao, W., Chen, L., Yuan, C., Chen, Q. and Kong, Q. (2022), “A novel electromechanical impedance-based method for non-destructive evaluation of concrete fiber content”, *Constr. Build. Mater.*, **351**, 128972. <https://doi.org/10.1016/j.conbuildmat.2022.128972>.
- Yuan, F.G., Zargar, S.A., Chen, Q., Wang, S., Zonta, D., Sohn, H., *et al.* (2020), “Machine learning for structural health monitoring: challenges and opportunities”, *Proceedings of Sensors and Smart Structures Technologies for Civil, Mechanical, and Aerospace Systems 2020*. <https://doi.org/10.1117/12.2561610>.
- Zagrai, A.N. and Giurgiutiu, V. (2001), “Electro-mechanical impedance method for crack detection in thin plates”, *J. Intell. Mater. Syst. Struct.*, **12**(10), 709-718. <https://doi.org/10.1177/104538901320560355>.